Nanostructures of Ionic Liquids Confined in Pores of SBA-15: Insights from Experimental Studies and Mean-Field Density Functional Theory

Nanostructure of Ionic Liquids Confined in Pores of SBA-15: Insights from Experimental Studies and Mean-Field Density Functional Theory

Dmitry N. Lapshin*[a], Andrei V. Gromov[b], Eleanor E. B. Campbell[b,c], Lev Sarkisov[d]

*[a] Institute for Materials and Processes, School of Engineering, University of Edinburgh, Robert Stevenson Road, Edinburgh EH9 3FB, United Kingdom. E-mail: Dmitry.Lapshin@ed.ac.uk.

[b] EaStCHEM, School of Chemistry, University of Edinburgh, David Brewster Road, Edinburgh EH9 3FJ, United Kingdom.

[c] School of Physics, Konkuk University, Seoul 05029, South Korea.

[d] Department of Chemical Engineering and Analytical Science, School of Engineering, University of Manchester, Manchester M13 9PL, United Kingdom.

Abstract

The arrangement of ionic liquids (ILs) within mesoporous ordered silica SBA-15 is revealed from nitrogen physisorption experiments combined with non-local density functional theory (NLDFT) analysis of pore structure and mean-field density functional theory (MFDFT). Using MFDFT on simple lattice models, we outline possible scenarios for IL distributions within the pores and conditions under which they originate. MFDFT predictions for nitrogen adsorption on these models of pore structures modified with ILs are in qualitative agreement with the experimental results. They demonstrate that the distribution of the ILs inside the pores of SBA-15 is sensitive to solid-fluid interactions, leading to different structures as a function of loading. This study also recommends the MFDFT and lattice models as a powerful framework for the interpretation of nitrogen sorption behavior, which complements the existing theoretical and experimental techniques to characterize the structure of **supported ionic liquids (SILs)**.

1. Introduction

Supported ionic liquid (SIL) materials are promising candidates for a broad range of applications, such as chemical synthesis,[1,2] catalysis,[3,4] batteries,[5] fuel and solar cells,[6] gas adsorption, and separation.[4] In these materials, the porous structure of the support is modified by depositing the ionic liquid (IL) inside its pores. The broad application of SILs is a result of several factors: i) they exhibit a unique combination of properties arising from both the support and the liquid; ii) ILs are good nonvolatile solvents with high ion mobility[7] and iii) they offer a broad range of chemistries due to various cation-anion combinations, hence their properties can be tuned for specific applications.[8]

One of the key factors that determines the application and efficiency of SILs is the state of the IL under confinement. The behaviour of confined ILs may depend on many factors: the solid-fluid interactions between the IL and the surface of the solid, the chemical heterogeneity of the surface, the chemical composition of the IL,[9] the method of deposition,[10] and the structure of the porous space.[10,11]

The interplay between electrostatic and dispersion interactions is critical for determining the precise arrangement of the ions at the surface of the pores and, therefore, for estimating the resulting properties of the confined IL that are challenging to predict.[12,13] Figure 1 schematically illustrates some possible states of the liquid confined in a pore. Each of these scenarios leads to a different performance of the material. For example, in our previous work,[14] we showed that if a film thinner than 2.5 nm forms in pores (Fig. 1(a)), the material exhibits strong gas adsorption properties with low gas selectivity. On the other hand, pores completely filled with IL (Fig. 1(b)) provide highly selective gas separation. Pores that are partially covered with nanodroplets (Fig. 1(c)) or isolated by liquid bridges (Fig. 1(d)) may cause unfavorable performance due to surface heterogeneity and reduced pore volume. In the latter case, significant volumes of the material become isolated due to the blockage of pores by ILs. Therefore, designing materials with an optimized performance requires an in-depth knowledge of the pore-filling mechanism and specific knowledge of the IL arrangement within the pores.

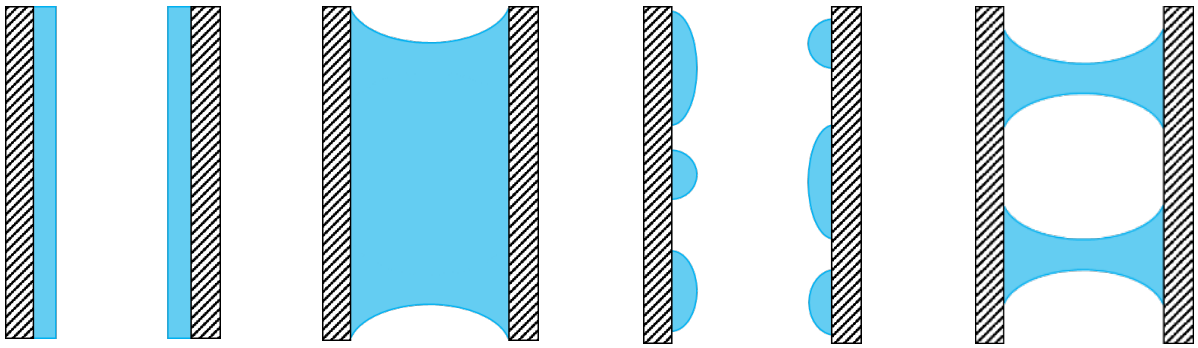

Figure 1. Possible scenarios of how ILs (blue area) distribute under confinement in a pore (dashed area indicates the pore walls): (a) the surface is uniformly covered with an IL layer; (b) the pore is completely filled with the IL; (c) IL nanodroplets cover the surface; (d) IL bridges form in the pore, isolating a portion of the pore.

Using the incipient wetness technique, Heinze *et al.* prepared and investigated several silica-based materials loaded with a range of ILs exhibiting low, medium, and high basicity.[9] In a series of detailed experimental studies involving nitrogen sorption, mercury intrusion, thermogravimetric analyses, and ^{129}Xe-NMR spectroscopy, they found that ILs based on acetate, $[CH_3CO_2]^-$ and trifluoromethanesulfonate, $[CF_3SO_3]^-$ anions wet the surface of ordered silica, MCM-41, and SBA-15, forming a homogeneous layer in the main mesopores. However, partial wetting of the surface or droplet formation was observed for ILs based on the bis(trifluoromethanesulfonyl)imide anion, $[Tf_2N]^-$. The authors found that the ILs start adsorbing in mesopores once they completely fill intrawall micro- and mesopores below a certain size.[9] The observed trends have also been reported for materials consisting of polymers deposited on the surface of the support.[15] In that study, Thommes and co-workers coated the surface of mesoporous silica SBA-15 and KIT-6 with hydrophilic poly(hydroxyethylmethacrylate) or hydrophobic polystyrene. Similar to ILs, a hydrophilic polymer first fills intrawall micro- and smaller mesopores, ultimately leading to a homogeneous polymer coating of the main mesopores. In contrast, a hydrophobic polymer does not exhibit any clear patterns and deposits as randomly dispersed inhomogeneous patches on the surface due to weak polymer-silica interactions. Solid-state NMR studies support the discussed observations with additional insights into the pore-filling mechanism. In particular, it was found that patches of the IL form on the pore surface of mesoporous silica (Silica 100) containing 1-ethyl-3-methylimidazolium

bis(trifluoromethylsulfonyl)imide, $[C_2C_1Im]^+[Tf_2N]^-$ at IL loadings below 10 vol.%.[16] Complete surface coverage with the IL is achieved for higher loadings.

Molecular simulation studies have also been used to explore the behaviour of ILs deposited in pores. Burt *et al*. studied the influence of the surface interaction potential between a graphene sheet and 1-butyl-3-methylimidazolium tetrafluoroborate, $[C_4C_1Im]^+[BF_4]^-$.[17] They demonstrated that weak liquid-solid interactions lead to droplet formation (partial wetting), while strong interactions promote uniform spreading of the IL over the surface. Partial wetting was also observed for silica surfaces.[18] In other studies, authors demonstrated that at low loadings, confined ILs, $[C_4C_1Im]^+[Tf_2N]^-$, $[C_2C_1Im]^+[Tf_2N]^-$ or $[C_2C_1Im]^+[SCN]^-$ form a monolayer or multilayers on the surface of mesoporous carbon nanotubes or silica.[19-22] At high loadings, the ILs completely fill mesopores. Some authors observed the formation of IL bridges that blocked portions of the mesopores.[19]

In spite of the progress outlined above in understanding the behaviour of confined ILs, there are still challenges that require further investigation. The most affordable, widely available, and convenient way to characterize porous materials, including SILs, is the physical adsorption of gases such as nitrogen or argon at cryogenic conditions. This technique produces an adsorption isotherm that requires further processing and interpretation to extract the information on the structure of the pores. In particular, pore size distribution (PSD) analysis can be presented as the following. The structure of the porous material is treated as a system of independent pores of a particular shape (slits, cylinders, spheres, or a combination of these shapes). A kernel of adsorption or desorption isotherms is produced using either the classical non-local density functional theory (NLDFT) or Monte-Carlo simulations. This is followed by solving the adsorption integral equation (AIE) to obtain the PSD compatible with the experimental data. NLDFT kernels and algorithms to solve the AIE are now a part of the standard software available with physical adsorption characterization equipment and used extensively to report PSD.[23] From Fig. 1 and the above discussion, it is clear that not all the scenarios shown in the figure will be easily amenable to this standard treatment simply because the structure of the SIL generally cannot be interpreted as a system of independent pores of a well-defined geometry. Typically, to comprehensively answer the question of the distribution of the ILs inside the porous structure, a spectrum of additional, more advanced techniques (such as electron microscopy, small-angle X-ray and neutron scattering, NMR, and infrared spectroscopy) is required, making the characterization process much more expensive and time-consuming. In this article, we show, by using the computationally efficient lattice mean-field density functional theory (MFDFT) approach to realistically model the distribution of the confined IL, that it is possible to obtain a qualitative interpretation of the distribution of IL inside porous materials from N_2 adsorption isotherms.

In recent decades, MFDFT has proved to be a useful framework for understanding the structure and thermodynamics of confined fluids and for pore structure characterization.[24] This theory allows one to model adsorption and desorption of fluid in a large variety of modelled materials and link the shape of the isotherm to the underlying structure, in other words, to the distribution of pores of these materials. For example, Monson *et al*. and Sarkisov *et al*. used MFDFT to explore metastable states of fluid in pores of different shapes and associated with them adsorption and desorption hysteresis observed in experimentally measured N_2 or Ar sorption isotherms.[25-26] Thus, by reproducing essential features of the experimental isotherm it is possible to reveal how, for example, the pore network, the pore heterogeneity, and the presence of narrow pores (necks) connected to large pores influence the

shape of the isotherm and the hysteresis loop.[27-29] Recently, MFDFT has been applied to calculate isotherms for a 3D-reconstructed ordered and disordered mesoporous silica that showed good qualitative agreement with the experimentally measured hysteresis loop and revealed the fluid morphology in that region.[30,31]

In this article we extend this approach by using MFDFT to construct a series of SIL models which can quickly produce a qualitative map of adsorption behaviours, resulting from different distributions of ILs in the pores. Specifically, we consider experimental N_2 adsorption isotherms for SBA-15 impregnated with two ILs exhibiting different interaction energies, 1-butyl-3-methylimidazolium hexafluorophosphate $[C_4C_1Im]^+[PF_6]^-$, and 1-ethyl-3-methylimidazolium bis(trifluoromethylsulfonyl)imide $[C_2C_1Im]^+[Tf_2N]^-$. The physical properties of these ILs are quite different with $[C_2C_1Im]^+[Tf_2N]^-$ exhibiting a higher density, lower viscosity, and lower surface tension than $[C_4C_1Im]^+[PF_6]^-$.[32,33] In addition, $[C_2C_1Im]^+[Tf_2N]^-$ shows a stronger tendency to crystallize on silica surfaces indicating stronger electrostatic interactions with silanol groups.[34] Samples of SBA-15 were loaded with different amounts of the two ILs. The resulting impregnated materials were first characterized using the conventional N_2 adsorption measurements to obtain the surface area, pore volume and PSD extracted using NLDFT. Two distinct trends in the N_2 isotherms for the two ILs were observed. By applying MFDFT to lattice models of SILs, we qualitatively reproduced the experimental N_2 isotherms and elucidated two distinct distribution scenarios for the studied ILs in SBA-15. This highlights the usefulness of theoretical tools such as the MFDFT in interpreting results from the physical adsorption characterization.

2. Experimental and Theoretical Methods

2.1. Materials

Mesoporous silica SBA-15 and ILs $[C_4C_1Im]^+[PF_6]^-$ and $[C_2C_1Im]^+[Tf_2N]^-$, were purchased from Sigma-Aldrich.

Mesoporous silica was impregnated with ILs using the incipient wetness technique.[4] Before impregnation, 200 mg of SBA-15 was activated at 120 °C under vacuum for at least 3 hours. The calculated amount of IL corresponding to a particular volumetric pore filling degree (δ = 0.1, 0.3, 0.5, and 0.9) was dissolved in methanol in a 100 ml round-bottom flask. Once the IL was dissolved, the activated powder of SBA-15 was mixed with the IL in the same flask. Next, the flask containing a suspension of SBA-15 in the methanol solution of the IL was attached to a rotary evaporator and then partially submerged in a water bath. The temperature of water in the bath was maintained at 50 °C. The rotary evaporator served to mix the silica and IL and to remove methanol at a reduced pressure of 250 mbar. Once all methanol was removed the obtained powder was further dried under vacuum at an elevated temperature of 80-90 °C. The resulting weight of the impregnated powder was within 3 % of the expected yield.

2.2. Nitrogen adsorption characterization with NLDFT

Gas physisorption analysis was conducted on a Quantachrome NOVA 3000 gas sorption analyzer. The implemented NLDFT models were supplied by the Quantachrome AsiQwin (version

3.01) software. Prior to the measurement, each sample was outgassed in a degas station under vacuum (< 1 mbar) at 90 ℃ for 12 hours to remove any adsorbed volatile species.

Pure and impregnated samples of SBA-15 were characterized by N_2 physisorption at 77 *K*. To establish the relationship between the structural characteristics of the porous material and the measured N_2 isotherms, we employed NLDFT. This method reconstructs the experimental isotherm by weighting a collection of individual isotherms (kernels) calculated for a family of pores of different sizes. Figures **S2** and **S3** in the Supplementary Information compare the experimentally measured N_2 isotherms at 77 *K* and isotherms calculated from NLDFT with the silica (SiO_2) and carbon (C) kernels for cylindrical pores. Isotherms measured for pure SBA-15 could be very well fitted by the model with just a small deviation at very low pressures (Fig S2(a)). Samples containing different amounts of $[C_4C_1Im]^+[PF_6]^-$ can be effectively described by the SiO_2-kernel, while samples modified with $[C_2C_1Im]^+[Tf_2N]^-$ are better described by the C-kernel at higher IL loadings. The IL $[C_2C_1Im]^+[Tf_2N]^-$ modifies the pore surface from siliceous to more carbonaceous because it more readily forms a monolayer on the silica surface.[34] Deviations at low pressure are more significant for all the impregnated samples. At this pressure, monolayer adsorption takes place, when all the adsorbed N_2 molecules are in contact with the surface of the adsorbent and, therefore, the presence of ions of the confined IL may alter the accuracy of the resulting fit. At higher pressures, where the gas condenses to a liquid-like phase in the mesopores and a hysteresis loop appears upon gas desorption, the fit is more accurate, implying a reliable description of the mesoporous structure.

Pore size distributions, free pore volumes (*V*), and specific surface areas (*S*) were obtained from both the adsorption and the desorption branches of isotherms of SBA-15 containing $[C_4C_1Im]^+[PF_6]^-$ by applying the SiO_2-kernel of (metastable) NLDFT adsorption isotherms and the kernel of (equilibrium) NLDFT desorption isotherms, respectively, considering an amorphous SiO_2 surface and a cylindrical pore model (Fig. S2).[23,35,36] The pore structure of SBA-15 impregnated with $[C_2C_1Im]^+[Tf_2N]^-$ was characterized using the SiO_2- and C-kernels of the (equilibrium) NLDFT desorption isotherm (Fig. S3). These results are presented in Fig. S4 and Table S1 of the Supplementary Information. The extracted PSDs, pore volumes and surface areas show only a minor difference between the results of different kernels, therefore, our further discussion is based on the results obtained from the desorption branch of the isotherms.

Previously, Ravikovitch and Neimark used NLDFT to characterize the pore structure of SBA-15 silica.[35] They found that it features a regular two-dimensional array of hexagonal (cylindrical) mesopores that are connected by a continuous network of irregular intrawall pores. From our measurements, the average width of the main mesopores is 7 nm. The size of intrawall pores ranges from micro- (< 2 nm) to mesopores (2-7 nm). The material has a well-developed surface area equal to 624-653 m^2/g and free pore volume equal to 0.710-0.725 ml/g.

Figure 2 shows typical plots of the cumulative surface area and pore volume for pure SBA-15 (black dash curves) and a sample containing 12.3 wt.% of IL $[C_4C_1Im]^+[PF_6]^-$ (solid red curves). The solid black curves show the cumulative surface area and pore volume of pure SBA-15 with the equivalent weight of SBA-15 for the sample containing IL. In other words, these curves represent what would be the cumulative surface area and volume of the SIL system if the properties of SBA-15 were

completely unaffected by the presence of the IL. Normalizing the behavior of pure SBA-15 (black dash curves) with respect to the weight of the SIL sample allows us to extract several useful properties.

Both the black and red curves show an almost evenly increasing surface area and pore volume up to 6 nm pore diameter. These pores are associated with the intrawall micro- and mesopores connected to the main mesopores with the mean pore diameter equal to 7 nm. An abrupt change in the surface area and volume of the main mesopores reflects a well-structured pore network, which mainly consists of 7 nm mesopores. The surface area and volume of the main mesopores are defined as shown in Fig. 2, and notation ΔS_1 and ΔV_1 is used for the normalized sample of pure SBA-15, while ΔS_2 and ΔV_2 is used for SBA-15 containing IL. By comparing quantities ΔS_1 to ΔS_2 and ΔV_1 to ΔV_2, it is possible to estimate the loss of the surface area and pore volume upon impregnation. For this, we calculate the respective quantities ($\Delta S_2/\Delta S_1$) and ($\Delta V_2/\Delta V_1$) that provide a clear indication of how the surface area and pore volume change with adding IL. From Fig. 2(b) the amount of the IL deposited in the main mesopores is equal to (ΔV_1-ΔV_2) in ml/g of the material. The amount of IL, which fills the intrawall pores is equal to ΔV_{iwall} and is determined as shown in Fig. 2(b). The obtained quantities allow us to explore the pore-filling mechanism separately for intrawall pores and the main mesopores and these are tabulated for all samples in Table S1 of the Supplementary Information and later discussed in Table 1.

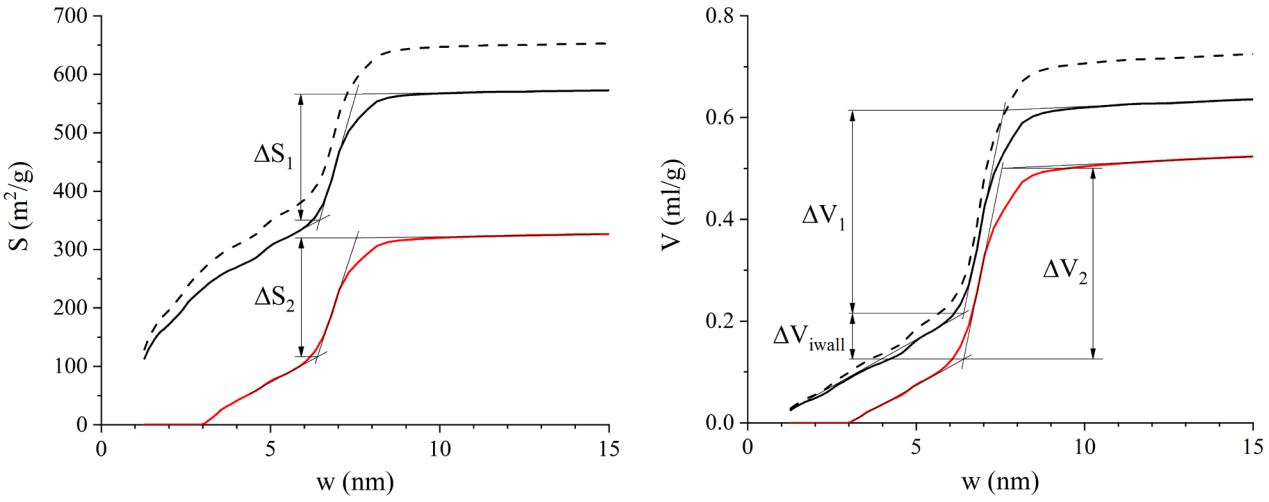

Figure 2. (a) Cumulative surface areas and (b) free pore volumes for the pure SBA-15 (black dash curves), the same sample normalized to the mass fraction (87.7 wt.%) of SBA-15 (solid black curves) of the SIL sample containing 12.3 wt.% of IL $[C_4C_1Im]^+[PF_6]^-$ (solid red curves). Quantities ΔS_1 to ΔS_2 and ΔV_1 to ΔV_2 show how the surface area and free pore volume for the main mesopores are calculated for the pure SBA-15 and the SIL sample respectively. ΔV_{iwall} defines the volume of intrawall pores filled with the IL for the SIL sample. All curves are determined from the desorption branches of the experimental isotherms by applying the SiO_2-kernel of the (equilibrium) NLDFT desorption isotherms considering an amorphous SiO_2 surface and a cylindrical pore model.

2.3. Mean-field density functional theory (MFDFT)

Mean-field density functional theory of lattice gas models has proved to be a powerful approach for the description of confined fluid phenomena.[26,29,37] In particular, this theoretical framework has

been of tremendous help in understanding the nature of the hysteresis loops for fluids confined in mesoporous structures.[24-26,37] Simple lattice models of porous structures and computationally efficient MFDFT were able to capture a diversity of metastable states and phase transitions of the confined fluid depending on the external conditions, such as temperature, chemical potential, and the strength of solid-fluid interactions. Moreover, MFDFT has been also extended to the dynamic behavior of fluids adsorbing in pores of various geometries.[25,27,38] In this section, we briefly overview key governing equations of MFDFT used in this work.

In lattice models, the physical space is represented by a system of discrete lattice sites. Each site can be either empty or occupied by a single fluid particle. This implies that all molecular size effects are excluded from the consideration. In the case of confined fluid problems, some of the lattice sites are also occupied by the adsorbent particles. Using this lattice sites formalism, one can consider porous structures of arbitrary complexity from simple slit pores to ink-bottle geometries to disordered porous glasses.[24] We also assume that particles interact only with the nearest-neighbor sites. The Hamiltonian for the lattice gas-solid system can be expressed as:

$$\mathcal{H} = -\frac{\varepsilon_{ff}}{2}\sum_{i<j} n_i n_j + \sum_i n_i \varphi_i \tag{1}$$

where n is the occupancy at site i and j and is equal to 1 if site i or j is occupied or 0 otherwise; $i < j$ denotes the sum over all the nearest-neighbour sites i and j; ε_{ff} is the nearest-neighbour fluid-fluid interaction energy; φ_i is the external field at site i, which describes the nearest-neighbour interaction between the fluid and the solid surface (ε_{sf}). The relation between the fluid-fluid and solid-fluid interactions is established via $\varepsilon_{sf} = \alpha\varepsilon_{ff}$.

Starting from the Hamiltonian in Equation (1) and using mean-field approximations, we can obtain an expression for the grand free energy:

$$\Omega(\{\rho_i\}) = kT\sum_i [\rho_i \ln(\rho_i) + (1-\rho_i)\ln(1-\rho_i)] - \frac{\varepsilon_{ff}}{2}\sum_{i<j}\rho_i\rho_j + \sum_i \rho_i(\varphi_i - \mu) \tag{2}$$

where $\{\rho_i\}$ is the set of densities for all the lattice sites in the system; $\rho_i = \langle n_i \rangle$ is the average density or occupancy at site i ranging from 0 to a maximum of 1 because of single occupancy; k is the Boltzmann constant; T is the temperature; μ is the chemical potential.

Equation (2) describes the thermodynamics of the confined fluid in equilibrium with the bulk fluid at a fixed chemical potential and constant temperature. The solution to this equation provides the density distribution, which minimizes the grand energy, $\Omega(\{\rho_i\})$ by applying the following condition:

$$\left(\frac{\partial\Omega}{\partial\rho_i}\right)_{\mu,V,T} = 0 \quad \forall\, i \tag{3}$$

where V is the volume of the system, which is related to the total number of lattice sites in the system within the MFDFT framework.

Combining Equation (2) with the condition of Equation (3) results in the following set of non-linear equations:

$$kTln\left(\frac{\rho_i}{(1-\rho_i)}\right) - \varepsilon_{ff}\sum_j \rho_j + \varphi_i - \mu = 0 \quad \forall\, i \tag{4}$$

This set of non-linear equations can be rearranged to give an expression for the average density on site i:

$$\rho_i = \frac{1}{(1+e^{-X_i})} \quad \forall\, i \tag{5}$$

where X_i is also derived from Equation (4):

$$X_i = \frac{1}{kT}\left[\varepsilon_{ff}\sum_j \rho_j - \varphi_i + \mu\right] \quad \forall\, i \tag{6}$$

The densities obtained from Equation (5) and plotted as a function of relative activity give the familiar adsorption and desorption isotherms for the lattice pore model. The relative activity λ/λ_0 where $\lambda = \exp(\mu/kT)$ can be expressed as

$$\frac{\lambda}{\lambda_0} = \exp\left(\frac{\mu^* + \mu_0^*}{T^*}\right) \tag{7}$$

where μ^* and T^* are the reduced chemical potential and temperature, equal to μ/ε_{ff} and kT/ε_{ff} respectively; λ_0 is the activity of the bulk lattice gas when no porous material or any adsorbent particles are present. Below the critical temperature T_c, where $T_c^* = kT_c/\varepsilon_{ff} = 1.5$ for a simple cubic lattice, a sparsely occupied gas phase coexists with a densely occupied liquid phase at the saturation chemical potential value $\mu_0 = {}^{n_c\varepsilon_{ff}}/_2 = -3\varepsilon_{ff}$ (where n_c is the coordination number, $n_c = 6$ for a cubic lattice), corresponding to the reduced saturation chemical potential value of $\mu_0^* = -3$.[24]

Similar to Equation (2), in the canonical ensemble at fixed density, volume, and temperature, the Helmholtz free energy can be expressed within the mean-field approximation as:

$$F(\{\rho_i\}) = kT\sum_i [\rho_i \ln(\rho_i) + (1-\rho_i)\ln(1-\rho_i)] - \frac{\varepsilon_{ff}}{2}\sum_{i<j}\rho_i\rho_j + \sum_i \rho_i\varphi_i \tag{8}$$

The necessary condition for a Helmholtz free energy minimum in the canonical ensemble is:

$$\left(\frac{\partial F}{\partial \rho_i}\right)_{N,V,T} - \mu = 0 \quad \forall\, i \tag{9}$$

which gives Equations (4) and (5). By solving Equation (5) with the imposed constraint of the constant overall density $\sum_i \rho_i = N$, the equilibrium density distribution and chemical potential (relative activity) can be obtained.

Using this framework, we have developed a model that captures the essential physics of adsorption in IL-modified pore systems. We model the distribution of a fluid representing an IL using canonical MFDFT, where the number of molecules (or overall density) remains fixed. This initial condition reproduces the experimental stage when a methanol solution containing some amount of IL completely fills the pores of SBA-15. Starting from some initial guess for the uniform distribution of density, one can allow the system to relax in order to minimize the Helmholtz free energy (Equation (9)). This should lead to some new, uneven distribution of density of the model IL in the pores, which will depend on the pore structure and on the relative strength of the solid-fluid and fluid-fluid interactions, α. In the experiment, this step would correspond to the evaporation of methanol leaving only IL deposited in pores. Although the concentration of IL in the methanol solution changes, the amount of IL molecules occupying the pores of SBA-15 remains constant. It is also important to acknowledge that the solution of Equation (9) may result in a local minimum, corresponding to a metastable state. This could also be the situation in experiments, where the final distribution of IL within the pores corresponds to some "stuck" metastable state. Hence, the numerical modelling of the IL distribution within the pores using MFDFT is conducted in the canonical ensemble with fixed fluid density at $T^* = 0.9$ and α equal to 0.75, 1.0, and 2.0 to simulate the partial and full wettability of the pore.[38]

The structures obtained from these calculations represent model distributions of the IL inside an SBA-15 material. These structures serve as an input to the second stage of the modelling process. Here, we model nitrogen adsorption on the IL-modified structures and calculate adsorption isotherms that now reflect the pore structure of these new complex systems. In nitrogen adsorption simulations we do not distinguish IL sites and pore wall sites. In other words, the strength of interaction between nitrogen and the IL is equal to that between nitrogen and the pore walls. Previously, Naumov *et al.* showed that chemical heterogeneity of pore walls influences only the low pressure region associated with the formation of a nitrogen monolayer, while it does not affect the shape of the hysteresis loop - the region of most interest to this study.[29] This allows us to model adsorption of nitrogen as a function of some geometrical changes in pores due to the presence of the confined IL. The appropriate statistical-mechanical framework to describe this adsorption process corresponds to the grand-canonical ensemble and solution of Equation (3). Using this equation, we obtain adsorption and desorption isotherms by varying the chemical potential of the adsorbing fluid. For this step, we use $T^* = 1.0$ and α equal to 3.0.[24] This temperature corresponds to 2/3 of the bulk critical temperature $T_c^* = 1.5$ for the simple cubic lattice gas in MFT. This fraction is comparable to that encountered in a nitrogen adsorption experiment near the normal boiling point, $T = 77\ K$. Adsorption and desorption isotherms obtained from these calculations are then compared to the experimental isotherms. The application of MFDFT to the lattice model is approximate, providing only a qualitative comparison with the experiment. However, if the shape of the hysteresis loop matches that from the experiment, the fluid morphologies from MFDFT will reflect the phenomena occurring in the real systems.[29] Detailed derivations of MFDFT and parameters for the MFDFT calculations are reported in the Supplementary Information.

2.4. Lattice pore models

From experimental studies of SBA-15, it is known that this material features cylindrical mesopores of size 5-30 nm and a continuous network of intrawall micro- and smaller mesopores

connecting these main mesopore channels.[39-41] The size of primary mesopores and the development of pore connectivity depend on the synthesis temperature, the procedure for the surfactant removal,[39] and the heat treatment.[42] In the construction of the lattice models of SBA-15, we have been inspired by the approach of Naumov *et al.*[29,43] This model captures all essential features of the real SBA-15 material, such as the main mesopore, some corrugation of its surface, and intrawall pore network. In particular, in this study, the structure of SBA-15 is represented by the serially connected pore model illustrated in Fig. 3(a).[44,45] The porous structure is formed by a linear chain of joined slit segments of different widths (Z) and equal length (X). The length of each segment is equal to 5 lattice sites, while the width varies randomly over the whole pore in such a way that the overall PSD obeys a Gaussian shape (Fig. 3(b)) with the mean width equal to 8 sites and the standard deviation equal to 0.5 sites. This diameter is large enough to observe different metastable states of the confined fluid and, at the same time, is small enough to capture fluid condensation at a pressure lower than the bulk liquid saturation pressure ($p/p_0 < 1$).[44] The intrawall pores are added with a random width every four segments as shown in Fig. 3(a). The width of intrawall pores along the x-direction has a uniform distribution from 2 to 6 lattice sites unless otherwise stated. The total number of segments is equal to $M = 500$. Therefore, the total number of intrawall pores is equal to $(M/4 - 1)$ respectively. The total length of the channel (L) is equal to the sum of the total lengths of all pore segments and intrawall pores along the x-axis. All systems considered in this work are in periodic boundary conditions in x- and z-directions and are infinite in the y-direction.

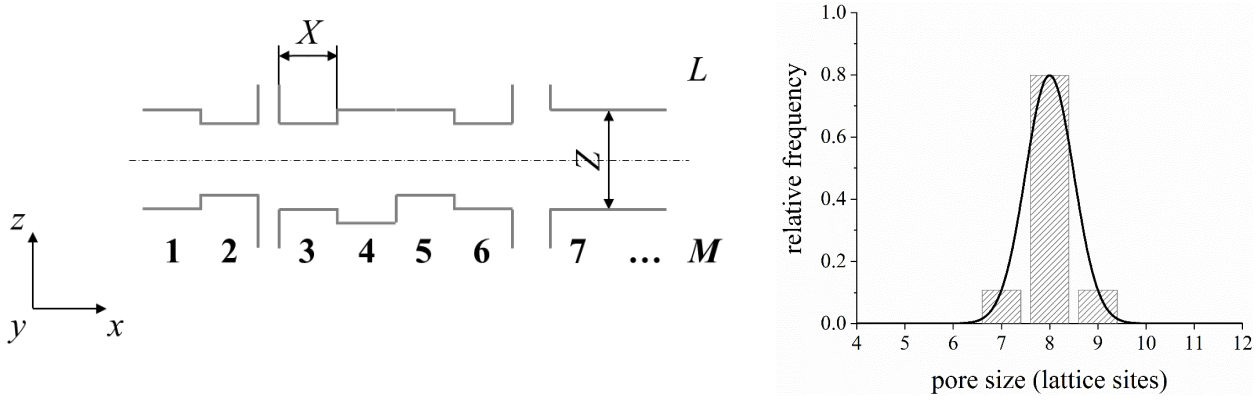

(a) (b)

Figure 3. (a) Schematic representation of a pore channel consisting of slit segments with the mean width $Z = 8$ sites and length $X = 5$ sites, connected to intrawall pores of different widths along the x-axis. The pore has periodic boundary conditions in x- and z-directions. (b) Pore size distribution of the pore channel without intrawall pores.

A visual inspection of the 3D-reconstructed SBA-15 obtained by electron tomography[31] and pore-filling process with fluid in[30] revealed that rough spots on the surface and pore constrictions in channels serve as adsorption sites for fluid. With this in mind, we use two types of the same lattice pore model with and without the pore constriction as shown in Fig. 4(a, b) to reconstruct the possible scenarios of IL adsorption in the real material. We realize that dead-ends may also be present in primary mesopores of SBA-15. However, we avoid their consideration because this would lead to significant complication of the lattice models in Fig. 4(a, b). In this case, the model would contain at least two parallel primary mesopores: i) mesopores open at both ends, and ii) mesopores split into two

close-ended mesopores. Simulations of IL adsorbing in the pore model result in different IL structures as shown in Fig. 4(c) where, for example, droplets may form in the main mesopore and some portion of IL may also fill smaller intrawall pores. By changing initial conditions (fluid density, temperature, strength of fluid-solid interactions) the IL may also deposit in the form of layers or liquid bridges. Our preliminary calculations of nitrogen adsorption and desorption isotherms for the systems in Fig. 4(a-c) placed in the periodic boundary conditions, led to the appearance of a broad hysteresis with the pore-emptying step at very low pressure. In the absence of a direct interface with the bulk gas phase or some other initial nucleus of the vapor phase, the system tends to get stuck in the metastable state until the limit of stability of the liquid nitrogen in the pore is reached.[29,46] To avoid this situation a single model pore containing IL and intrawall pores (Fig. 4(c)) was surrounded by a bulk gas layer of 10 lattice sites (Fig. 4(d)). This model has a finite length (L) and is used for the studies of nitrogen adsorption (Fig. 4(d)) and desorption (Fig. 4(e)) processes. The contact with the bulk gas is essential for a correct description of equilibrium evaporation of liquid-like condensate in an open pore in Fig. 4(e). In particular, this model allows us to catch the development of vapor-liquid interfaces (represented by receding menisci) on the desorption branch of the hysteresis loop.[30]

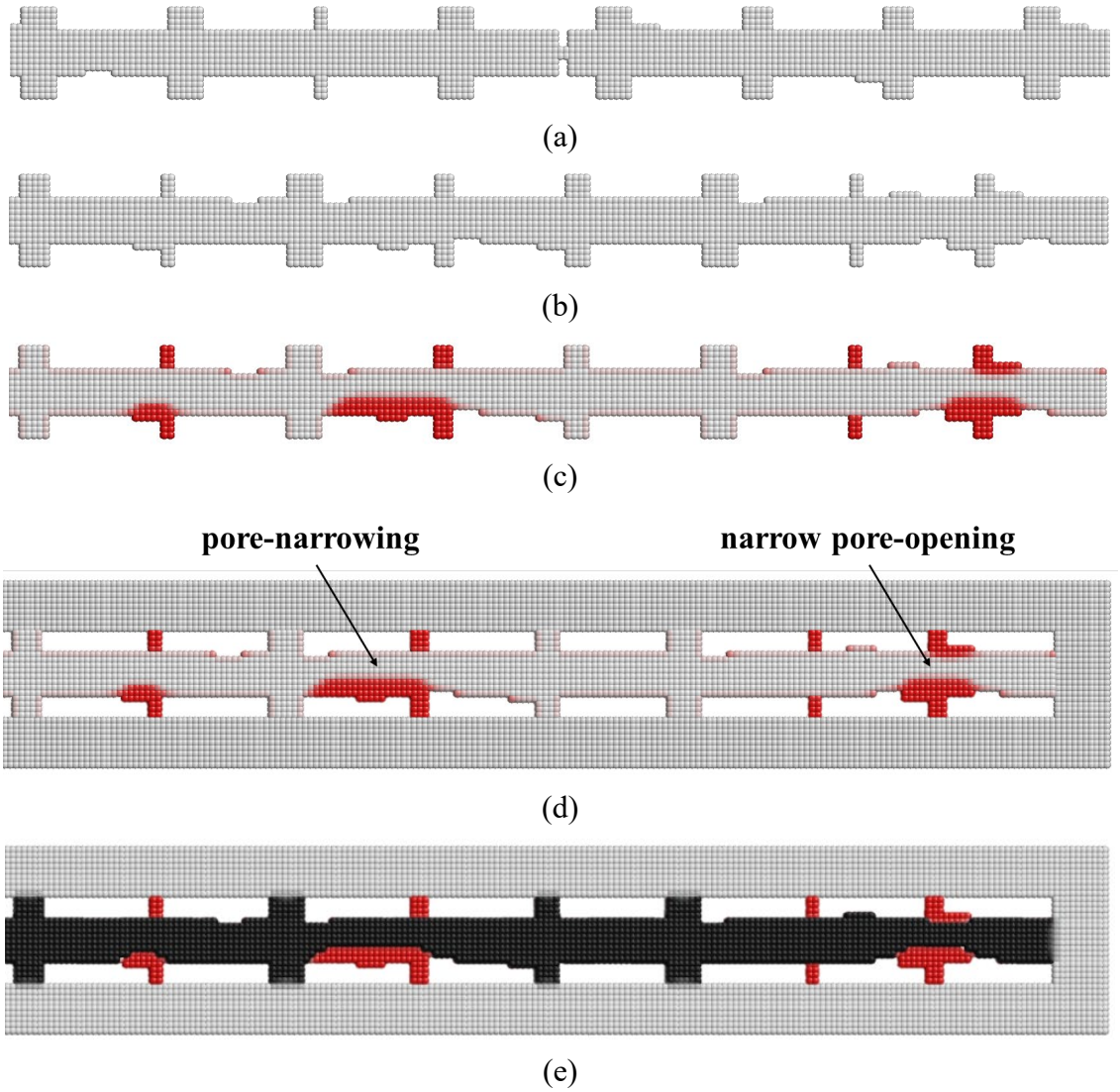

Figure 4. Lattice pore models used in this study: (a, b) the infinite empty pore channels with one pore constriction placed in the middle of the pore and without it respectively and used for adsorption of IL

in the canonical ensemble; (c) the infinite pore containing adsorbed IL (red lattice sites), which further serves as the input pore for nitrogen adsorption and desorption calculations in (d); (d) the pore of finite length with pre-adsorbed IL used for nitrogen adsorption and surrounded by the bulk gaseous nitrogen; red droplets of IL reduce the width of the mesopore leading to the appearance of pore narrowings within the mesopore body, while narrow pore openings appear at both ends of the pore and provide access to the bulk gas; (e) the pore of finite length with pre-adsorbed IL containing adsorbed nitrogen (black lattice sites) and surrounded by the bulk gaseous nitrogen. For (d) and (e) only the right side of the pore is shown. The width of intrawall pores ranges from 2 to 6 lattice sites. Adsorption and desorption of nitrogen are conducted in the grand canonical ensemble. The lattice sites for IL and N_2 are shaded using 10 shades of red and gray respectively with darker shades denoting higher densities.

In the system containing IL, we may anticipate hysteresis phenomena associated with how the IL modifies the pore geometry and network topology. A vivid example of how the pore geometry and network change is presented in Fig. 4(c) and (d). Here, droplets of IL modify the mesopore leading to the appearance of pore narrowings and narrowing down the existing pore openings connecting the pore space to the bulk gas as illustrated in Fig.4(d). The intrawall pores are also filled with the IL. Therefore, we may envision a situation when the main mesopore has no other access to the bulk gas phase other than through pore-narrowings. From the perspective of the desorbing nitrogen, this system corresponds to the ink-bottle geometry and some pore blocking or cavitation effects would be expected depending on how narrow the pore openings have become.[36] Similarly, if IL bridges form in the main mesopore it is possible to anticipate the disappearance of the hysteresis loop due to advanced adsorption.[28] Later in the work, we will consider these situations in more detail and discuss how these pore network effects can be related to particular distributions of confined ILs at different conditions.

3. Results and Discussion

3.1. Nitrogen sorption experiments

The N_2 adsorption and desorption isotherms for SBA-15 impregnated with ILs $[C_4C_1Im]^+[PF_6]^-$ and $[C_2C_1Im]^+[Tf_2N]^-$ are presented on a linear scale in Fig. 5(a) and (b), respectively, for different IL loadings. All isotherms are of type IV(a) that feature an H1 hysteresis.[47] The fit (black and red curves) calculated from NLDFT as described above is accurate for the higher pressure region, where the hysteresis loop is observed, and less accurate for low-pressure adsorption, where fluid-solid interactions are susceptible to the chemical composition of the surface. The location, shape, and size of the hysteresis loop contain information about the mesopore structure and its connectivity via the intrawall network. The main objective of the experimental part of the study is to extract this information and propose possible pore-filling mechanisms for the two ILs confined in the main mesopores and intrawall pores, using standard NLDFT.

According to Fig. 5(a) filling silica pores with different amounts of IL $[C_4C_1Im]^+[PF_6]^-$ does not change the shape and location of the hysteresis loop, but only reduces the amount of N_2 adsorbed due to the loss of the free pore volume. In contrast, in the $[C_2C_1Im]^+[Tf_2N]^-$ impregnated samples, the hysteresis loop shifts to lower pressure as the loading of the IL increases (the vertical dashed guidelines in Fig. 5(b) help to see this effect).

To understand the pore-filling mechanism, we analyze how the cumulative surface area, free pore volume, and PSD change as pores of SBA-15 are filled with the gradually increasing amount of the IL. Here, a fraction of the pore volume occupied by the IL is defined as the pore-filling degree (δ) and is equal to $V_{IL} / V_{SBA\text{-}15}$, where $V_{SBA\text{-}15}$ is the volume of pure SBA-15 normalized to the mass fraction of SBA-15 of the corresponding SIL sample as was described for the case presented above in Fig. 2. This analysis is presented in Table 1 and Fig. 5(c) and (d) for the desorption branch of the isotherms shown in Fig. 5(a) and (b). Each sample containing a certain volume of IL (V_{IL}), is characterized by its total surface area (S_{total}) and pore volume (V_{total}) measured in the experiment. Impregnation of IL into the porous support leads to the loss of the surface area ($\Delta S_2/\Delta S_1$) and volume ($\Delta V_2/\Delta V_1$) of the main mesopores. Depending on the local structure of the mesopores and pore network, the IL may block some fraction of the mesopores due to liquid bridging. To find out whether the prepared samples contain blocked volume (V_{block}), we compare V_{total} to V_{free}. Volume V_{free} is defined as the expected free pore volume calculated as the difference between the free volume of pure SBA-15 and the volume of the IL taken for impregnation. If these values are close to each other, then V_{block} approaches 0 %. According to the table, we conclude that the pore volume of all samples is accessible to nitrogen (V_{block} < 5 %). The IL also fills intrawall micro- and mesopores. As discussed in the Methodology section, ΔV_{iwall} gives the amount of IL present in these intrawall pores, while (ΔV_1-ΔV_2) corresponds to the volume of IL present in the main mesopores. Hence, the sum ΔV_{iwall} + (ΔV_1-ΔV_2) should be equal to the total volume of added IL (V_{IL}). Any small difference between these two values can be attributed to experimental errors and/or the use of the room temperature IL density for calculating the volume.

3.1.1. SIL $[C_4C_1Im]^+[PF_6]^-$

Table 1 (samples 1-4) summarizes the effects of filling SBA-15 with IL $[C_4C_1Im]^+[PF_6]^-$. Filling about 21 vol.% of the free pore volume with $[C_4C_1Im]^+[PF_6]^-$ does not change the surface area ($\Delta S_2/\Delta S_1 \approx 100$ %) and pore volume ($\Delta V_2/\Delta V_1 \approx 100$ %) of the main mesopores. Importantly, the amount of IL added to SBA-15 (V_{IL}) is almost equal to the free volume of intrawall pores and of the main mesopores lost upon impregnation ΔV_{iwall} + (ΔV_1-ΔV_2). Together with PSDs in Fig. 5(c), we argue that the main mesopores are not filled with the IL, while the intrawall micro- and mesopores gradually become filled resulting in the loss of the corresponding pore volume. It is also possible that rare patches of IL may randomly form in the main mesopore, which do not affect the overall shape of the isotherm and PSD. Adding more IL significantly changes the porosity of sample 4, where half of the pore volume is filled with the IL. The first noticeable change is in the surface area and pore volume of the main mesopores that reduce equally by almost 50 %. Furthermore, the main peak in the PSD does not change its position and shifts only downward relative to samples 1-3 indicating that some portion of the mesopores is completely filled with the IL, while the remaining portion is empty. This analysis allows us to hypothesize a plausible pore-filling mechanism for SBA15 and $[C_4C_1Im]^+[PF_6]^-$, which is schematically illustrated in Fig. 5(e). At low loadings (steps 1 and 2), the IL fills intrawall micro- and mesopores without altering the morphology and chemical composition of the main mesopores. Simultaneously, some rare patches of IL may form in the main mesopore (step 3). At a higher loading (step 4) the IL forms a liquid bridge in the main mesopores which spreads along the pore.

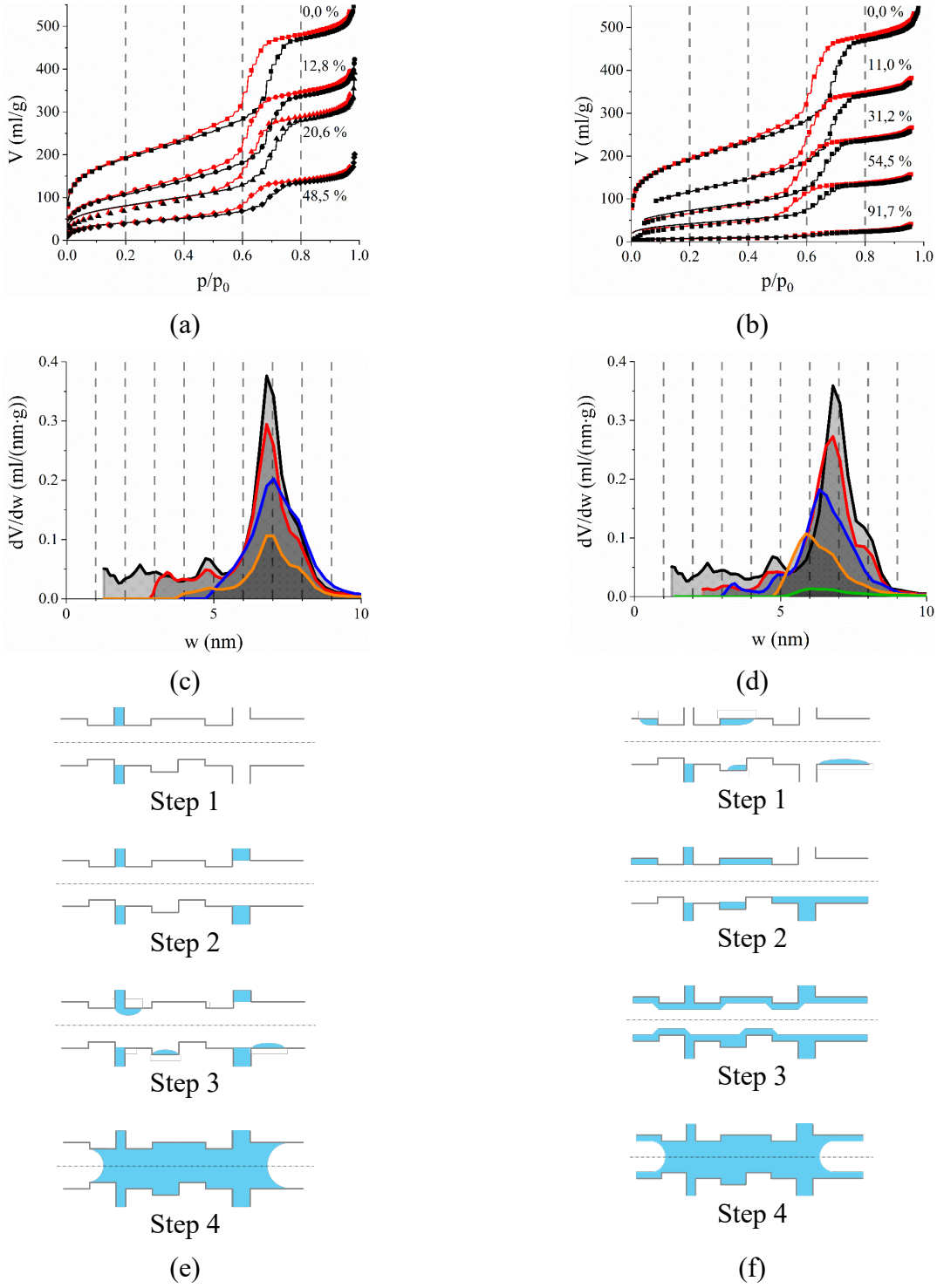

Figure 5. (a) and (b) Nitrogen adsorption and desorption isotherms measured at 77 *K* for SBA-15 impregnated with IL, $[C_4C_1Im]^+[PF_6]^-$ or $[C_2C_1Im]^+[Tf_2N]^-$ respectively for different pore filling degrees. Dots are the experimental results; lines are the fitted isotherms obtained from NLDFT with a kernel for silica and carbon cylindrical pore shape; black and red colors correspond to adsorption and desorption branches of the isotherm. (c) and (d) NLDFT pore size distributions obtained from desorption isotherms of pure SBA-15 (black), and filled with the IL for the following pore filling degrees (c) $[C_4C_1Im]^+[PF_6]^-$ - 12,8 % (red), 20.6 % (blue), 48.5 % (orange); and (d) $[C_2C_1Im]^+[Tf_2N]^-$ - 11.0 % (red), 31.2 % (blue), 54.5 % (orange), 91.7 % (green). (e) and (f) Illustrations of the hypothesized pore filling mechanism for $[C_4C_1Im]^+[PF_6]^-$ and $[C_2C_1Im]^+[Tf_2N]^-$, respectively.

Table 1. Pore structure characterization of SBA-15 impregnated with $[C_4C_1Im]^+[PF_6]^-$ or $[C_2C_1Im]^+[Tf_2N]^-$.

#	Composition,		V_{IL}	V_{SBA-15}	S_{total}	ΔS_1	ΔS_2	$\frac{\Delta S_2}{\Delta S_1}$	V_{total}	ΔV_1	ΔV_2	$\frac{\Delta V_2}{\Delta V_1}$	V_{free}	ΔV_{iwall}	$\Delta V_{iwall} + (\Delta V_1 - \Delta V_2)$	V_{block}	δ
	SBA-15	IL	*ml/g*	*ml/g*	m^2/g	m^2/g	m^2/g	%	*ml/g*	*ml/g*	*ml/g*	%	*ml/g*	*ml/g*	*ml/g*	%	*vol.%*
$[C_4C_1Im]^+[PF_6]^-$																	
1	1.000	0.000	-	0.725	653	-	-	-	0.725	-	-	-	0.725	-	-	0,0	0.0
2	0.877	0.123	0.090	0,636	326	216	202	94	0.523	0.400	0.375	94	0.546	0.088	0.113	3.55	12.8
3	0.816	0.185	0.135	0,591	240	204	210	103	0.437	0.369	0.390	106	0.456	0.174	0.153	3.15	20.6
4	0.653	0.347	0.254	0,473	121	161	84	52	0.212	0.291	0.156	54	0.219	0.128	0.263	1.47	48.5
$[C_2C_1Im]^+[Tf_2N]^-$																	
5	1.000	0.000	-	0.710	624	-	-		0.710	-	-	-	0.710	-	-	0.0	0.0
6	0.894	0.106	0.070	0,635	406	198	191	96	0.534	0.396	0.363	92	0.565	0.066	0.099	4.93	11.0
7	0.748	0.252	0.166	0,531	228	167	168	101	0.369	0.331	0.289	87	0.366	0.119	0.161	-0.62	31.2
8	0.630	0.370	0.244	0,447	128	139	124	89	0.210	0.278	0.197	71	0.203	0.155	0.236	-1.38	54.5
9	0.503	0.497	0.328	0,357	20	112	17	15	0.036	0.222	0.030	13.5	0.030	0.125	0.317	-1.85	91.7

3.1.2. SIL[C_2C_1Im]$^+$[Tf_2N]$^-$

We now explore how the IL [C_2C_1Im]$^+$[Tf_2N]$^-$ deposits inside SBA-15. The most notable difference in comparison to adsorption of [C_4C_1Im]$^+$[PF_6]$^-$ is that the main peak in the PSDs (Fig. 5(d)) gradually shifts from 7 to 6 nm as the pore filling degree (δ) increases from 11 to 92 vol.%. At a low loading corresponding to δ = 11 vol.%, the main peak in the PSD broadens and negligibly shifts by 0.11 nm (Fig. 5(d)) alluding to random adsorption of small ion pairs at active sites that perturb the morphology of the main mesopores. The presence of these small IL patches does not significantly change the surface area and mesopore volume of the support as shown in Table 1 (sample 6). This means that most of the IL fills a fraction of intrawall pores with a size of less than 5 *nm* as evidenced from a rough equality of V_{IL} and V_{iwall} in Table 1(sample 6) and a downward shift of the PSD curve Fig. 5(d).

Further addition of the IL (Table 1 (sample 7)) reduces the available mesopore volume ($\Delta V_2 < \Delta V_1$), although the surface area does not change ($\Delta S_2 \approx \Delta S_1$). To propose a mechanism for IL adsorption, we investigate the relation between the surface area and volume for the cylindrical pore and the thickness of the adsorbed IL layer. (see Supplementary Information). These calculations are based on the assumption that the IL uniformly covers the surface of the pore. Applying Equation (**S27**) to sample 7, we derive the average thickness of the adsorbed IL layer to be equal to 0.25 nm. The main peak in the PSD (Fig. 5(d)) shifts by 0.5 nm to a smaller pore width, which is consistent with the 0.25 nm thickness of the film. However, the physically meaningful value of the monolayer is approximately equal to 0.5 nm.[4,48] These results imply that the IL covers the surface of the main mesopores non-uniformly with a monolayer of approximately 0.5 nm thickness leaving some portions of the surface area uncovered.

At a higher loading (Table 1 (sample 8)) the IL completely fills intrawall pores and covers the surface of mesopores with a monolayer as evidenced from a reduction of the surface area and free pore volume. Using the relation (**S27**) in the Supplementary Information, we find that a uniform monolayer with a thickness of 0.5 *nm* forms in the main mesopores. Additionally, the main peak in Fig. 5(d) shifts by 1.0 *nm* confirming the monolayer formation.

Finally, at the highest loading, we observe significant changes in the porous structure of the impregnated sample 9 (Table 1). In particular, the surface area and pore volume equally reduce by about 85 % resulting in almost complete filling of the main mesopores with the IL. The PSD diagram (green curve) in Fig. 5(d) does not shift with respect to the diagram for sample 8 (orange curve). It seems that once a monolayer is formed, further pore filling proceeds through the formation of a liquid bridge and its growth along the pore.

Based on the analysis above, we propose a different pore-filling mechanism for SBA-15 and [C_2C_1Im]$^+$[Tf_2N]$^-$, which is schematically illustrated in Fig. 5(f). At low loadings, the IL fills a portion of intrawall pores and also randomly adsorbs on active sites of the main mesopores (step 1). At higher loadings, the IL completely fills smaller intrawall pores and partially covers the surface of mesopores with a monolayer (step 2), which eventually spreads over the whole surface area (step 3). Once the IL completely covers the surface, further addition of the IL induces the formation of the liquid bridge in the main mesopores, which then grows along the pore (step 4).

3.2. Mean-field density functional theory calculations

The observed differences in the two pore filling mechanisms in Fig. 5(e) and (f) are most likely due to different relative strengths of the surface and liquid interactions, α. To test this hypothesis, we use numerical simulations based on MFDFT. Usually, this theory is used to study the underlying principles of N_2 or Ar sorption at 77 or 87 *K* to explain metastability of fluid under confinement in the region of the hysteresis loop and to extract information about the pore structure of different materials.[27,29,31,44,49-51] Here, we adopt MFDFT to study the adsorption of ILs in the canonical ensemble. The important implication of this approach is that it allows us to change the relative strength of solid-fluid and fluid-fluid interactions and, therefore, directly observe possible scenarios of fluid (IL) distribution in pores. Applying the same theory to these hypothetical systems already containing IL, we calculate N_2 adsorption and desorption isotherms in the grand-canonical ensemble and use them to explain the trends observed in the experiments.

Figure 6 provides the isotherms calculated from MFDFT for N_2 adsorption in and desorption from model pores containing different amounts of IL. Pore size distributions of the main mesopore and intrawall pores are shown in the bottom panels. The amount of confined IL is expressed as a relative density of lattice sites occupied by the IL (red sites in visualizations) to the total number of lattice sites in the pore. Our preliminary calculations showed difficulty in finding solutions for MFDFT in the canonical ensemble (Equation (9)) when a high density of IL is initialized. Therefore, in Fig. 6 we do not consider cases for high IL loadings. Visualizations of two representative sections of the pore model illustrate the behavior of the IL at a particular loading in intrawall micro- and mesopores and in the main mesopore.

3.2.1. Non-wetting IL (α = 0.75)

For the case where the IL partially wets the surface of the pore (α = 0.75),[46] we used a lattice pore model with intrawall pores ranging in size from 2 to 6 lattice sites and with an increased fraction of 6-sites intrawall pores to avoid delayed desorption effects as discussed in section 2.4. According to Fig. 6(a) and (d) adsorption of the IL does not influence the shape and location of the N_2 hysteresis loop (top panels). These theoretical isotherms qualitatively agree with N_2 sorption experiments for SBA-15 impregnated with $[C_4C_1Im]^+[PF_6]^-$. This important result implies that the behavior of the IL derived from MFDFT is representative of the real behavior of the IL confined in SBA-15. At a low loading (0.078), the IL fills only small intrawall pores as indicated from the corresponding PSD and visualization (Fig. 6(a)). At higher loadings (0.110-0.133) the IL starts to fill larger intrawall pores and forms droplets on the surface of the main channel. The presence of droplets does not change the PSDs of the main channel. These results support our tentative proposition earlier on that rare patches of $[C_4C_1Im]^+[PF_6]^-$ may randomly form in the main mesopores as illustrated in step 3 in Fig.6(e). Further addition of IL (0.271) leads to complete filling of small intrawall pores with a width of less than 5 lattice sites. Moreover, the IL creates multiple liquid bridges that completely fill some portions of the pore. The presence of the 2-site constriction in the main channel (Fig. 6(d)) does not influence the pore filling mechanism except that this narrowing serves as an additional active site initiating IL bridging at low IL loading (0.089). In spite of the presence of IL bridges all unfilled sections of the mesopore have access to the bulk gas surrounding the pore through wide intrawall pores.

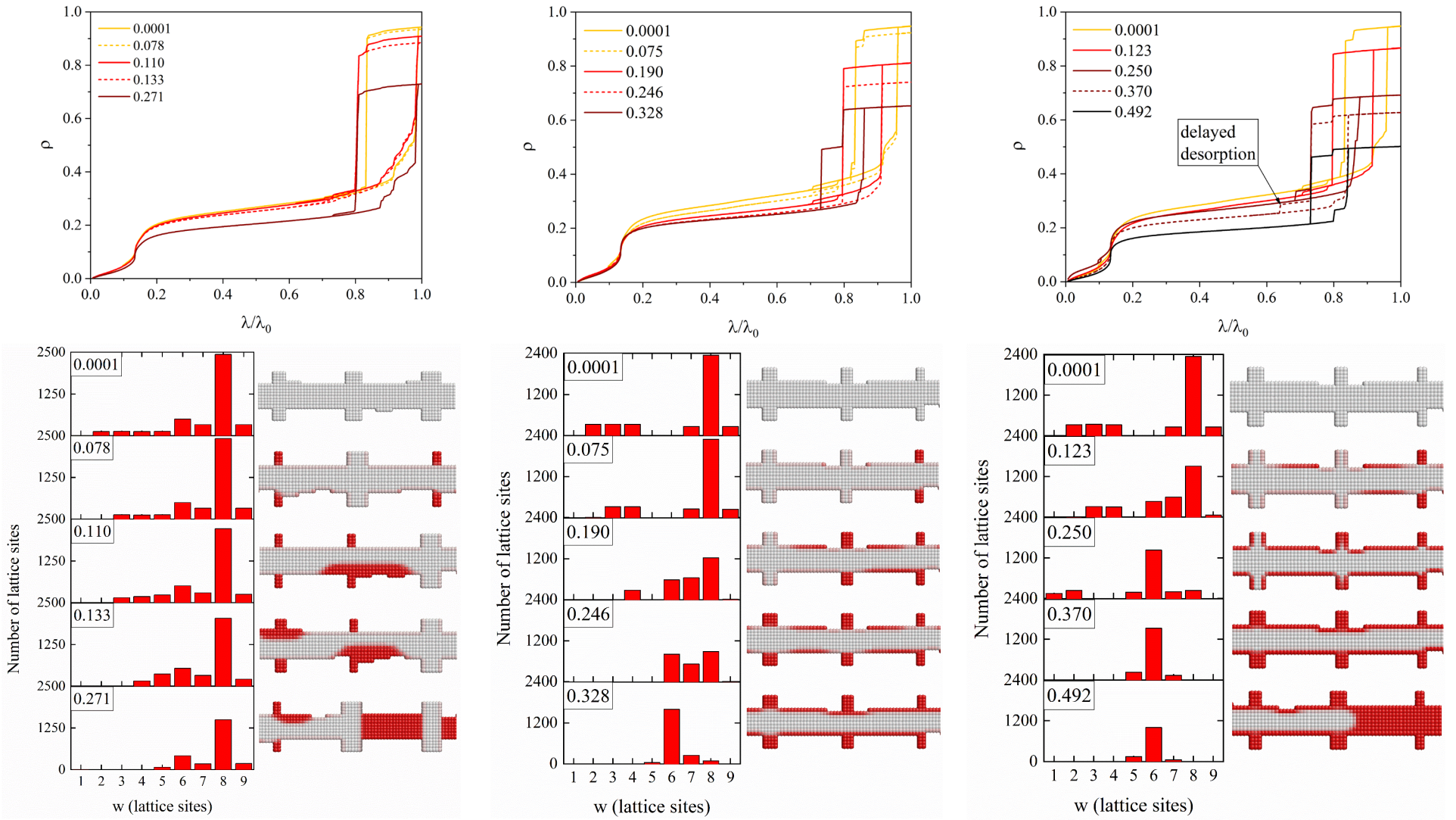
0.0001
0.078
0.110
0.133
0.271
ρ
λ/λ0
Number of lattice sites
w (lattice sites)
(a)
0.0001
0.075
0.190
0.246
0.328
(b)
0.0001
0.123
0.250
0.370
0.492
delayed
desorption
(c)

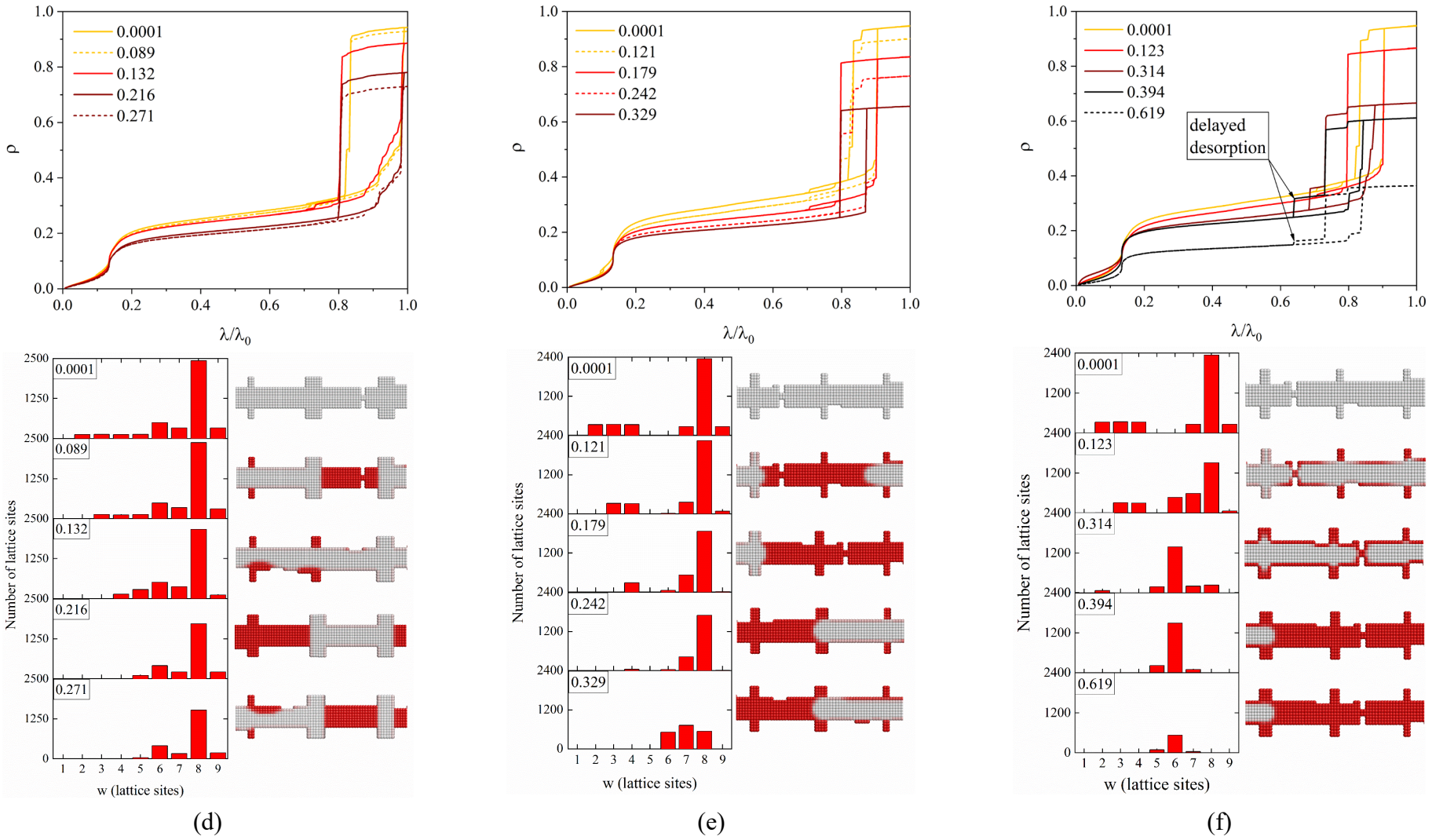

Figure 6. Density isotherms or average fractional occupancy (top panels) for the lattice model of N_2 in slit pores without (a-c) and with (d-f) a single pore constriction and also containing pre-adsorbed IL. Bottom panels contain PSDs at different IL loadings and corresponding visualizations of slit pores. Visualizations illustrate how ILs are distributed at different loadings and the strengths of interaction, α: (a, d) 0.75, (b, e) 1.0, (c, f) 2.0. Each visualization shows some representative sections of the pore channel to illustrate the specific behavior of ILs at a particular loading (hence, the choice of the visualized section may change from loading to loading in the panels above).

3.2.2. Well-wetting IL (α = 1.0 and 2.0)

To study the adsorption of ILs with relatively stronger liquid-solid interactions (α = 1.0 and 2.0) we used a lattice pore model with a uniform distribution of intrawall pores with the size of 2-4 lattice sites. Our preliminary simulations revealed that including larger intrawall pores leads to additional effects, not seen in experiments. In particular, the isotherms exhibited delayed desorption or multiple condensation steps in the order of the increasing diameter of intrawall pores. These isotherms are presented in Fig. S6.

In comparison to partially wetting ILs, adsorption of stronger surface interacting ILs (α = 1.0, 2.0) proceeds through a different mechanism shown in Fig. 6(b, e) and (c, f). At low loadings (yellow curves), the IL tends to fill intrawall pores without affecting the morphology of the main mesopore channel that is reflected in minor changes of hysteresis loops. Increasing the amount of added IL (red curves) leads to partial adsorption of the IL on active sites (undulated regions) of the surface. The PSD becomes smoother and the N_2 hysteresis loop shifts to lower relative activity (relative pressure). An additional amount of IL spreads over the surface completely covering the surface with a monolayer (dark red curves). Interestingly, once a monolayer is formed, further addition of the IL leads to the appearance of a single liquid bridge (black curves), which grows along the channel. The presence of the constriction in the main channel induces IL bridging at lower IL loading as seen in Fig. 6(e, f). Once the liquid bridge forms in the main mesopore, the pore on each side of the bridge becomes essentially a closed-ended slit pore model.[24,28] For the system with α = 1.0, there is parity between liquid-solid and liquid-liquid interactions which results, on the one hand, in liquid bridging, and, on the other hand, in partial coverage of the surface with the monolayer at higher IL density equal to 0.329 as shown in visualization in Fig. 6(e)). As a result of forming the monolayer, the mean size of the pore channel reduces from 8 to 6 lattice sites and the hysteresis loop is shifted to lower relative activity in the nitrogen adsorption studies. These results indicate that the changes in the theoretical isotherms and PSDs are qualitatively similar to those observed in the experiment for samples of SBA-15 impregnated with $[C_2C_1Im]^+[Tf_2N]^-$ (Fig. 5(b, d)). Importantly, the pore-filling mechanism revealed by MFDFT in Fig. 6(c, f) reproduces the proposed mechanism in Fig. 5(f) derived from the experiment.

3.3.3. Pore-network effects

In addition to reproducing essential features of experimental isotherms for impregnated silica and revealing the pore-filling mechanism, the applied MFDFT calculations, and created lattice pore models allow us to correlate the shape of N_2 isotherms to the pore network effects. In particular, we can explore under what conditions i) portions of the main channels can become isolated; and ii) advanced adsorption and pore-blocking can occur.

Firstly, the main channel can have access to the bulk vapor phase either directly or indirectly through the network of intrawall micro- and mesopores. Having these intrawall channels filled with the IL isolates the main channels from each other, and in the current models this happens if the intrawall pores have the width of 4 lattice sites or less. For these conditions, there are two possible effects. The first one is the isolation of some portions of the main channel due to the formation of multiple liquid bridges. In this case, the isolated volume is not accessible to nitrogen molecules and the resulting pore volume measured in experiments will be significantly reduced. In the second case,

the IL adsorbed in the main channel may form constrictions leading to the ink-bottle shape of the pore. In nitrogen sorption experiments, this newly-formed shape of the pore induces the cavitation effect and associated with it a delayed nitrogen desorption isotherm.[28] In Fig. 6(c, f) we observe a pronounced tail in the desorption isotherms at $\lambda/\lambda_0 = 0.65$ for pore models containing a wetting IL (α = 2.0) at densities 0.370 and 0.394 respectively. Figure 7 visualizes a region of the pore containing IL at a density of 0.370 (Fig. 6(c)) where delayed desorption is observed (a similar situation is observed for the sample containing 0.394 of IL from Fig. 6(f)). This region is isolated from the bulk gas phase because all intrawall pores of widths 2-4 sites are filled with the IL (red sites). Moreover, the monolayer of the IL creates pore narrowings with the width of 4 sites at both sides of the region. These newly-formed pore-narrowings delay emptying of the pore via the cavitation effect. In this example, the cavitation effect is minor and can be seen by the presence of less dense fluid in wide segments of the pore. These results show that the MFDFT simulations can effectively be used to explain the reasons for observing delayed desorption of nitrogen at 77 *K* for adsorbents containing an IL. Although our experimental isotherms for SBA-15 do not show any delayed desorption, this effect cannot be excluded for other materials with a different pore structure. Furthermore, the two described effects, i.e. pore isolation due to liquid bridging and formation of pore constrictions or narrowings can be eliminated if the pore network is well developed and consists of wide intrawall pores. In application to SBA-15, the material should have a narrow mesopore size distribution, such that the diameter of intrawall pores and the main mesopores is the same.

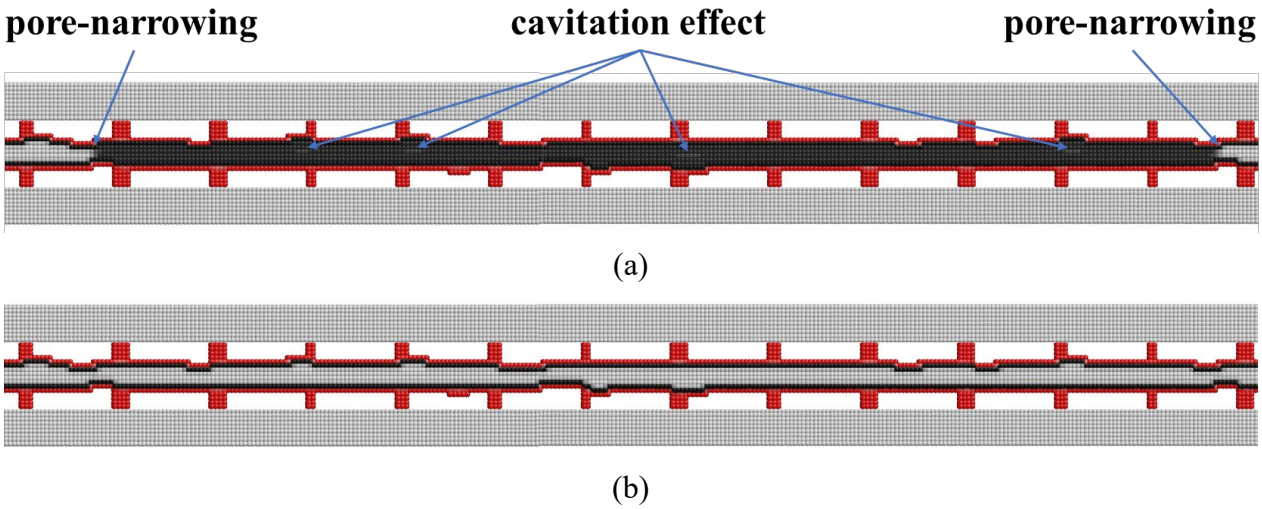

Figure 7. Visualizations of fluid density states in the lattice pore model with the mean width of the main mesopore 8 lattice sites and uniformly distributed widths of intrawall pores from 2 to 4 lattice sites surrounded by the gas phase. Visualizations show desorption of N_2 (black sites) from the pore containing pre-adsorbed IL (red sites) with density 0.370 in Fig. 6(c): (a) μ^* = -3.445; (b) μ^* = -3.450. Cavitation effect points to the bubbles of slightly lower density (dark grey in (a)) inside the pore segments filled with nitrogen.

Previously, Monson and Sarkisov found that nitrogen adsorption in close-ended pores proceeds through an equilibrium phase change, thus, eliminating the hysteresis loop.[24,28] This implies that the IL bridges present in SILs may also influence the shape of the hysteresis loop measured in N_2 sorption experiments. To test this hypothesis, we modelled two lattice pores shown in Fig. S7. They consist of a single slit pore of a length of 200 sites and a width of 8 sites closed at one end. The model in Fig.

S7(b) also has a narrowing with a width of 6 sites. These close-ended pores can be considered as pores containing the IL bridge.

Figure 8 depicts nitrogen sorption isotherms calculated for these two models. The black isotherm exhibits a very narrow hysteresis loop indicating that adsorption and desorption of the fluid correspond to the equilibrium phase change, which is the characteristic of the close-ended pores. Interestingly, the pore narrowing changes the desorption curve (red curve) and shifts the equilibrium phase transition to a lower relative pressure, which agrees with the desorption from a pore with a width of 6 sites. A detailed analysis of pore filling and emptying in Fig. S7 clearly shows that the narrowing leads to a pore-blocking effect. This implies that even if the pore is closed at one end the presence of narrowings or surface undulations created by the confined IL will lead to the appearance of the hysteresis loop. This explains why in the experiment we observe the hysteresis loop for samples where IL bridges form.

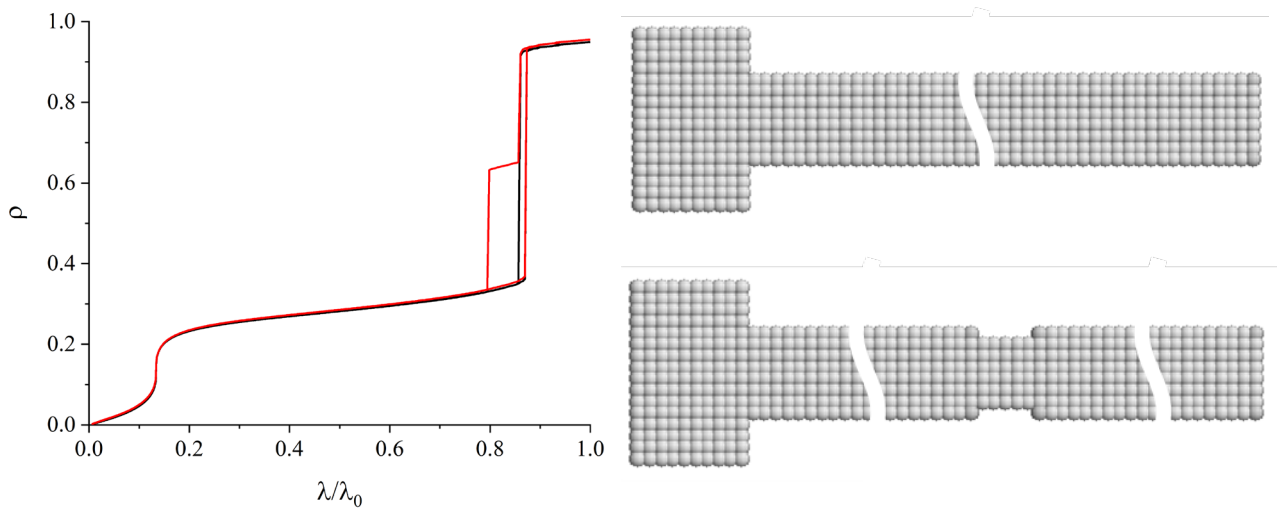

Figure 8. Density isotherms or average fractional occupancy (left panel) for the lattice model of N_2 in slit pores of 8-sites width without (black) and with (red) a single pore narrowing of 6-sites width as shown in the right panel. The whole length of pore models is shown in Fig. S7 of the Supplementary Information.

Let us now assume that the red isotherm in Fig. 8 is measured in the experiment. The analysis of the adsorption branch would yield a PSD corresponding to the pore width of 8 sites. In contrast, the desorption branch would yield two peaks at widths of 8 and 6 sites. The influence of the pore-blocking effect on the resulting PSD is well-known and has been investigated extensively for SBA-15 by Guillet-Nicolas and co-authors.[52] However, in our experiments we obtain similar PSDs obtained from the adsorption and desorption branches of the isotherms for SBA-15 impregnated with $[C_4C_1Im]^+[PF_6]^-$. Considering the broad diversity of structures that ILs may form under confinement, this issue requires further investigation that will be pursued in future research.

4. Conclusions

Ionic liquids confined in porous materials exhibit complex behaviour that is different from the bulk behaviour and is challenging to predict. Using nitrogen sorption experiments combined with an advanced pore structure characterization technique based on NLDFT, we determined correlations between changes in the surface area and pore volume of silica material SBA-15 and possible structures of the confined IL deposited inside pores. This allowed us to hypothesize two different step-by-step pore-filling mechanisms that explain the adsorption behaviour of the two contrasting ILs. Using MFDFT calculations for a lattice model of a single mesopore with a network of intrawall pores, we explored the two proposed pore-filling hypotheses. Importantly, we showed that the theory qualitatively reproduces experimental nitrogen isotherms and PSDs, thus, providing plausible confirmation of our hypotheses. We found that the key factor influencing the pore-filling mechanism is the relative strength of liquid-solid interactions compared to liquid-liquid interactions and, to a lesser extent, the presence of surface undulations and constrictions that serve as active sites of adsorption for ILs.

According to our findings, adsorption of IL $[C_4C_1Im]^+[PF_6]^-$ is described by weak surface-liquid interactions over much stronger liquid-liquid interactions $\alpha = 0.75$, and proceeds through filling the smaller intrawall pores and partial wetting of the main pore when rare IL patches randomly form on the surface. Finally, multiple liquid bridges form and grow in size, reducing the available pore volume. Adsorption of this IL negligibly changes the chemistry and inner structure of mesopores, hence, does not affect the position of the main peak in the PSD. In contrast, the IL $[C_2C_1Im]^+[Tf_2N]^-$ deposits on the silica surface through a different mechanism governed by strong surface-liquid interactions $\alpha > 1$. Along with filling the intrawall pores, the IL wets the surface covering it with a monolayer. This shifts the maximum of PSD to lower pore widths. Finally, the IL forms a single liquid bridge, which continually spreads along the pore as the amount of added IL increases.

Using MFDFT simulations we also provide an explanation of possible pore-blocking and cavitation effects induced by the deposited IL. We argue that these effects depend not only on the size of the main mesopores but to a significant extent on the structure of the intrawall pore network. Indeed, for a system with narrow intrawall pores filled with IL, we observed a scenario where additional network effects manifest themselves during the nitrogen desorption process as a result of the IL in the main channel creating ink-bottle-like segments. Although **some of** these effects have not been observed experimentally, the MFDFT points to their possibility and the required conditions.

Finally, we demonstrated that the applied MFDFT approach provides a useful and simple framework to guide the interpretation of nitrogen sorption experiments. Being computationally efficient, MFDFT and lattice models can be used to quickly chart a map of possible behaviors of ILs in the porous system. It also provides additional insights into complex pore network effects complementing the available experimental techniques. Furthermore, we envision that these simple models are employed to propose new structures with specific adsorptive behavior to guide the experimental synthetic campaign in a search for more efficient materials and promising applications.

Conflicts of interest

There are no conflicts to declare.

Supporting Information

Additional experimental N_2 adsorption and desorption isotherms at 77 *K* and pore structure charecterization results for studied SILs. Additional results on MFDFT calculations for different pore networks.

Acknowledgments

This work was supported by the Edinburgh Global Research Scholarship and the Principal's Career Development PhD Scholarship. This work has made use of the resources provided by the Edinburgh Compute and Data Facility (ECDF) (http://www.ecdf.ed.ac.uk/). Eleanor E. B. Campbell acknowledges financial support from EPSRC FlexiICCS (EP/N024613/1). The authors thank Prof. P. Monson (University of Massachusetts, Amherst) for sharing the MFDFT code used in the reported studies.

References

1. Welton, T. Room-temperature ionic liquids. Solvents for synthesis and catalysis. *Chem. Rev.* **1999**, *99*, 2071-2084.

2. Blanchard, L. A.; Hancu, D.; Beckman, E. J.; Brennecke, J. F. Green processing using ionic liquids and CO_2. *Nature* **1999**, *399*, 28-29.

3. Zhao, H.; Holladay, J. E.; Brown, H.; Zhang, Z. C. Metal chlorides in ionic liquid solvents convert sugars to 5-hydroxymethylfurfural. *Science* **2007**, *316*, 1597-1600.

4. Fehrmann, R.; Riisager, A.; Haumann, M. *Supported Ionic Liquids: Fundamentals and Applications*; Wiley-VCH: Weinheim, 2014.

5. Ohno, H. *Electrochemical Aspects of Ionic Liquids*; Wiley: Hoboken, 2005.

6. Bai, Y.; Cao, Y.; Zhang, J.; Wang, M.; Li, R.; Wang, P.; Zakeeruddin, S. M.; Grätzel, M. High-performance dye-sensitised solar cells based on solvent-free electrolytes produced from eutectic melts. *Nat. Mater.* **2008**, *7*, 626-630.

7. Rogers, R. D.; Seddon, K. R. Ionic liquids-solvents of the future? *Science* **2003**, *302*, 792-793.

8. Krossing, I.; Slattery, J. M. Semi-empirical methods to predict the physical properties of ionic liquids: an overview of recent developments. *Z. Phys. Chem.* **2006**, *220*, 1343-1359.

9. Heinze, M. T.; Zill, J. C.; Matysik, J.; Einicke, W. D.; Gläser R.; Stark, A. Solid-ionic liquid interfaces: pore filling revisited. *Phys. Chem. Chem. Phys.* **2014**, *16*, 24359-24372.

10. Hayes, R.; Warr G. G.; Atkin, R. At the interface: Solvation and designing ionic liquids. *Phys. Chem. Chem. Phys.* **2010**, *12*, 1709-1723.

11. Horn, R. G.; Israelachvili, J. N. Direct measurement of structural forces between two surfaces in a nonpolar liquid. *J. Chem. Phys.* **1981**, *75*, 1400-1411.

12. Rane, K. S.; Errington, J. R. Understanding the influence of Coulomb and dispersion interactions on the wetting behavior of ionic liquids. *J. Chem. Phys.* **2014**, *141*, 174706-174716.

13. Perkin, S. Ionic liquids in confined geometries. *Phys. Chem. Chem. Phys.* **2012**, *14*, 5052-5062.

14. Lapshin, D. N.; Jorge, M.; Campbell, E. E. B.; Sarkisov, L. On competitive gas adsorption and absorption phenomena in thin films of ionic liquids. *J. Mater. Chem. A* **2020**, *8*, 11781-11799.

15. Guillet-Nicolas, R.; Wainer, M.; Marcoux, L.; Thommes, M.; Kleitz, F. Exploring the confinement of polymer nanolayers into ordered mesoporous silica using advanced gas physisorption. *J. Colloid Interface Sci.* **2020**, *579*, 489-507.

16. Haumann, M.; Schonweiz, A.; Breitzke, H.; Buntkowsky, G.; Werner, S.; Szesni, N. Solid-state NMR investigations of supported ionic liquid phase water-gas shift catalysts: ionic liquid film distribution vs. catalyst performance *Chem. Eng. Technology* **2012**, *35*, 1421-1426.

17. Burt, R.; Birkett, G.; Salanne, M.; Zhao, X. S. Molecular dynamics simulations of the influence of drop size and surface potential on the contact angle of ionic-liquid droplets. *J. Phys. Chem. C* **2016**, *120*, 15244-15250.

18. Castejon, H. J.; Wynn, T. J.; Marcin, Z. M. Wetting and tribological properties of ionic liquids. *J. Phys. Chem. B* **2014**, *118*, 3661-3668.

19. Bañuelos, J. L.; Feng, G.; Fulvio, F.; Li, S.; Rother, G.; Dai, S.; Cummings, T.; Wesolowski, D. J. Densification of ionic liquid molecules within a hierarchical nanoporous carbon structure revealed by small-angle scattering and molecular dynamics simulation. *Chem. Mater.* **2014**, *26*, 1144-1153.

20. Rajput, N. N.; Monk, J.; Singh, R.; Hung, F. R. On the influence of pore size and pore loading on structural and dynamical heterogeneities of an ionic liquid confined in a slit nanopore. *J. Phys. Chem. C* **2012**, *116*, 5169-5181.

21. Pensado, A. S.; Malberg, F.; Gomes, M. F. C.; Padua, A. A. H.; Fernandez, J.; Kirchner, B. Interactions and structure of ionic liquids on graphene and carbon nanotubes surfaces. *RSC Adv.* **2014**, *4*, 18017-18024.

22. Li, S.; Han, K. S.; Feng, G.; Hagaman, E. W.; Vlcek, L.; Cummings, T. Dynamic and structural properties of room-temperature ionic liquids near silica and carbon surfaces. *Langmuir* **2013**, *29*, 9744-9749.

23. Landers, J.; Gor, G. Yu.; Neimark, A. V. Density functional theory methods for characterization of porous materials. *Colloids and Surfaces A: Physicochem. Eng. Aspects* **2013**, *437*, 3-32.

24. Monson, P. Understanding adsorption/desorption hysteresis for fluids in mesoporous materials using simple molecular models and classical density functional theory. *Microporous and Mesoporous Materials* **2012**, *160*, 47-66.

25. Monson, P. Mean field kinetic theory for a lattice gas model of fluids confined in porous materials. *J. Chem. Phys.* **2008**, *128*, 084701-084710.

26. Kierlik, E.; Monson, P.; Rosinberg, M. L.; Sarkisov, L.; Tarjus, G. Capillary condensation in disordered porous materials: Hysteresis versus equilibrium behavior. *Phys. Rev. Lett.* **2001**, *87*, 055701-055704.

27. Edison, J. R.; Monson, P. Dynamic mean field theory of condensation and evaporation in model pore networks with variations in pore size. *Microporous and Mesoporous Materials* **2012**, *154*, 7-15.

28. Sarkisov, L.; Monson, P. Modeling of adsorption and desorption in pores of simple geometry using molecular dynamics. *Langmuir* **2001**, *17*, 7600-7604.

29. Naumov, S.; Valiullin, R.; Kärger, J.; Monson, P. Understanding adsorption and desorption processes in mesoporous materials with independent disordered channels. *Physical Review E* **2009**, *80*, 031607-031615.

30. Svidrytski, A.; Rathi, A.; Hlushkou, D.; Ford, D. M.; Monson, P.; Tallarek, U. Morphology of fluids confined in physically reconstructed mesoporous silica: Experiment and mean field density functional theory. *Langmuir* **2018**, *34*, 9936-9945.

31. Svidrytski, A.; Hlushkou, D.; Thommes, M.; Monson, P.; Tallarek, U. Modeling the impact of mesoporous silica microstructures on the adsorption hysteresis loop. *J. Phys. Chem. C* **2020**, *124*, 21646-21655.

32. Dzyuba, S. V.; Bartsch, R. A. Influence of structural variations in 1-alkyl(aralkyl)-3-methylimidazolium hexafluorophosphates and bis(trifluoromethylsulfonyl)imides on physical properties of the ionic liquids. *Chem.Phys.Chem.* **2002**, *3*, 161-166.

33. Shi, B. The strengths of van der Waals and electrostatic forces in 1-alkyl-3-methylimidazolium ionic liquids obtained through Lifshitz theory and Coulomb formula. *Journal of Molecular Liquids* **2020**, *320*, 114412-114417.

34. Zhang, S.; Zhang, J.; Zhang, Y.; Deng, Y. Nanoconfined ionic liquids. *Chem. Rev.* **2017**, *117*, 6755-6833.

35. Ravikovitch, P. I.; Neimark, A. V. Characterization of micro- and mesoporosity in SBA-15 materials from adsorption data by the NLDFT method. *J. Phys. Chem. B* **2001**, *105*, 6817-6823.

36. Thommes, M.; Cychosz, K. A. Physical adsorption characterization of nanoporous materials: progress and challenges. *Adsorption* **2014**, *20*, 233-250.

37. Woo, H.-J.; Sarkisov, L.; Monson, P. A. Mean-field theory of fluid adsorption in a porous glass. *Langmuir* **2001**, *17*, 7472-7475.

38. Edison, J. R.; Monson, P. Dynamic mean field theory of condensation and evaporation processes for fluids in porous materials: Application to partial drying and drying. *Faraday Discuss.* **2010**, *146*, 167-184.

39. Kruk, M.; Jaroniec, M.; Ko, C. H.; Ryoo, R. Characterization of the porous structure of SBA-15. *Chem. Mater.* **2000**, *12*, 1961-1968.

40. Zhao, D.; Feng, J.; Huo, Q.; Melosh, N.; Fredrickson, G. H.; Chmelka, B. F.; Stucky, G. D. Triblock copolymer syntheses of mesoporous silica with periodic 50 to 300 angstrom pores. *Science* **1998**, *279*, 548-552.

41. Zhao, D.; Huo, Q.; Feng, J.; Chmelka, B. F.; Stucky, G. D. Nonionic triblock and star diblock copolymer and oligomeric surfactant syntheses of highly ordered, hydrothermally stable, mesoporous silica structures. *J. Am. Chem. Soc.* **1998**, *120*, 6024-6036.

42. Kruk, M.; Antochshuk, V.; Matos, J. R.; Mercuri, L.; Jaroniec, M. Determination and tailoring the pore entrance size in ordered silicas with cage-like mesoporous structures. *J. Am. Chem. Soc.* **2002**, *124*, 768-769.

43. Naumov, S.; Khokhlov, A.; Valiullin, R.; Kärger J.; Monson, P. Understanding capillary condensation and hysteresis in porous silicon: Network effects within independent pores. *Phys. Rev. E* **2008**, *78*, 06061-06064.

44. Kikkinides, E. S.; Monson, P.; Valiullin, R. Sorption isotherm reconstruction and extraction of pore size distributions for serially connected pore model (SCPM) structures employing algorithmic and statistical models. *J. Phys. Chem. C* **2020**, *124*, 21591-21607.

45. Salmas, C. E.; Stathopoulos, V. N.; Pomonis, J.; Rahiala, H.; Rosenholm, J. B.; Androutsopoulos, G. An investigation of the physical structure of MCM-41 novel mesoporous materials using a corrugated pore structure model. *Appl. Catal. A* **2001**, *216*, 23-40.

46. Monson, P. Contact angles, pore condensation, and hysteresis: insights from a simple molecular model. *Langmuir* **2008**, *24*, 12295-12302.

47. Thommes, M.; Kaneko, K.; Neimark, A. V.; Olivier, J. P.; Rodriguez-Reinoso, F.; Rouquerol, J.; Sing, K. S. W. Physisorption of gases, with special reference to the evaluation of surface area and pore size distribution (IUPAC Technical Report). *Pure Appl. Chem.* **2015**, *87*, 1051-1069.

48. Wandelt, K. *Surface and Interface Science*; Wiley-VCH: Weinheim, 2020.

49. Coasne, B.; Gubbins, K. E.; Pellenq, R. J.-M. Domain theory for capillary condensation hysteresis. *Phys. Rev. B* **2005**, *72*, 024304-024312.

50. Morishige, K. Dependent domain model of cylindrical pores. *J. Phys. Chem. C* **2017**, *121*, 5099-5107.

51. Schneider, D.; Valiullin, R. Capillary condensation and evaporation in irregular channels: Sorption isotherm for serially connected pore model. *J. Phys. Chem. C* **2019**, *123*, 16239-16249.

52. Guillet-Nicolas, R.; Bérubé, F.; Thommes, M.; Janicke, M. T.; Kleitz, F. Selectively Tuned Pore Condensation and Hysteresis Behavior in Mesoporous SBA-15 Silica: Correlating Material Synthesis to Advanced Gas Adsorption Analysis. *J. Phys. Chem. C* **2017**, *121*, 24505-24526.

Table of Contents

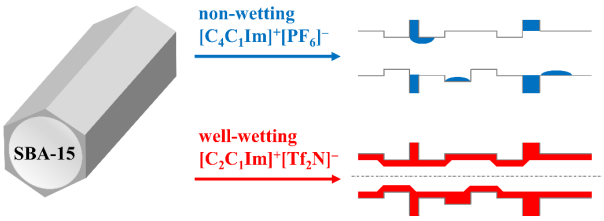

Mean-field density functional theory provides a powerful framework for the interpretation of nitrogen sorption experiments at 77 K for pore structure characterization of supported ionic liquids.